Characterization of Controlled Flow Separation

C. J. Peterson, B. Vukasinovic, and A. Glezer

Woodruff School of Mechanical Engineering, Georgia Institute of Technology, Atlanta, GA 30332-0405.

Abstract

Inherent flow separation within a diffuser duct is delayed using fluidic actuation, and the dynamics and structure of the natural and migrated separation ($M_o = 0.4$) in the absence and presence of actuation, respectively, are investigated experimentally. Specifically, the flow features within measurement domains localized near separation are explored using conditional averaging, spectral analysis, and proper orthogonal decomposition. Variable actuation input by an integrated array of fluidic oscillating jets migrates the separation downstream through the imposed adverse pressure gradient. The time-averaged velocity distributions of both the natural and migrated separation are dominated by the presence of a shear layer away from the surface while the shear stress at the surface diminishes and vanishes approaching separation. The present investigations show that by extending flow attachment via flow control, the characteristic cross stream scale of the separating velocity distribution increases significantly and develops an additional inflection point close to the surface. Regardless of the distinct differences in cross stream scales of the mean velocity between the base and controlled flows, scaling by outer shear layer parameters yields a reasonable global collapse of the velocity profiles for both flow conditions, except very close to the surface. A combined outer and inner shear layer scaling is shown to further improve the collapse compared to the outer scaling alone. Conditional averaging of the flow fields highlights an overall increase in the turbulent kinetic energy levels as separation migrates under flow control compared to the base flow. Spectra of the velocity fluctuations about the migrated separation exhibit an increase in the energy of the large-scale motions that is coupled to a transfer to small scales at lower frequencies than in the base flow. Proper orthogonal decomposition analysis is used to explore the underlying flow structure through separation in the absence and presence of actuation. The modal decomposition indicates that despite the pronounced increase in low frequency energy, the local vorticity modes in the natural and migrated separation are remarkably similar, and simply undergo tilting and stretching as the separation is forced to migrate downstream.

American Institute of Aeronautics and Astronautics

I. Background

Internal flow in compact, aggressive flow diffuser ducts is susceptible to local separation at the inlet of the secondary ducts, owing to strong adverse pressure gradients. The incipient separation at the inlet, which can persist throughout the branched duct, results in flow instabilities and significant losses in both duct sections that may compromise system scale and weight. Active flow control offers a potential for mitigating the adverse effects of the internal flow separation by delaying the onset of separation well into the imposed adverse pressure gradient.

The severe losses that are associated with internal flow separation have motivated numerous investigations of the fundamental aspects of these complex flows over the years in various geometries that share characteristic form features with branched ducts, such as flow junctions (e.g., Ethier, et al., 2000), convex banks (Blanckaert, 2015), backward facing steps (Papadopoulos and Otugen, 1995), and curved ducts (Yang et al., 2006), to name a few. Investigations of active control of internal flow separation have received considerable attention since the 1950s. Nishi et al. (1998) investigated control of flow separation over a conical diffuser by vortex-generating jets and reported an optimum jet-to-free stream velocity ratio between 1.5 and 2 for an overall minimum total pressure loss coefficient of approximately 0.3 in the diffuser. Suzuki et al. (2004) considered flow separation in a two-dimensional diffuser and its control by periodic mass injection. Their reduced-order model study showed alteration of vortex formation and dynamics in the controlled flows that led to a reduction of the separation bubble albeit with negligible changes in the separation location. Studies by Amitay et al. (2002) demonstrated the effectiveness of active flow control in delaying internal separation in a duct having a rectangular cross section, and reported a reduction in the streamwise scale of the separation domain and concomitant increase in the volume flow rate and reduction in losses in the presence of flow actuation. In a related investigation, Kumar and Alvi (2006) demonstrated feasibility of another flow control element, a high-speed micro-jet, for suppressing flow separation at $M < 0.2$. Banaszuk et al. (2003) demonstrated the application of an adaptive flow control scheme for multi-frequency flow separation control in a planar diffuser by utilization of synthetic jets. Vaccaro et al. (2015) investigated mitigation of internal flow separation in a compact rectangular offset duct using steady blowing at the flow boundary (up to $M \approx 0.45$) and showed that changes in flow attachment can affect total pressure recovery and distortion in the affected flow segment. More recently, Gartner and Amitay (2015) compared the effect of sweeping, pulsed, and two-dimensional jet actuation on pressure recovery in a transonic rectangular diffuser and showed that sweeping jets could produce higher pressure recovery at comparable mass flow rates. In an investigation of hybrid flow control that encompasses the use of control jets coupled with a passively trapped vorticity concentration at the flow boundary of an offset high-speed subsonic diffuser, Burrows et al. (2016) demonstrated suppression of the secondary vortices by actuation-effected changes in the topology of the trapped vortex and hence significantly suppressed distortion at the diffuser outlet.

In addition to the time-invariant effects of flow control on the nominally time-averaged spatial delay (or displacement) of the separation, another important aspect of the actuation is its effect on the flow dynamics about the new location of separation which can have significant impact on global flow stability. In a review of aspects of turbulent flow separation, Simpson (1989) noted that a defining characteristic of separated flow is the large turbulent stress within the separated shear layer that is associated with the formation of large-scale vortices that effect pressure fluctuations and coupled unsteady pressure-velocity oscillations in the recirculating flow domain.

The effects of separation control on the unsteady flow features of flow separation reattachment are of particular interest. Chun and Sung (1996), Yoshioka et al., (2001) and Vukasinovic et al. (2010) investigated control of separating flow at a fixed separation point, formed by an abrupt change in the flow boundary over a backward-facing step. Chun and Sung (1996) demonstrated that acoustic forcing near the separation point had significant effect on the characteristics of the separated flow structure by altering the roll-up of the forming vortices and thereby varying entrainment and, ultimately, the reattachment length downstream of the step. Yoshioka et al. (2001) showed that the effects of actuation on flow reattachment downstream of the backward-facing step increased production of the Reynolds stresses. Vukasinovic et al. (2010) attributed the increased turbulent kinetic energy production and dissipation within the separated shear layer to high-frequency (dissipative) actuation at the location of separation. Marusic and Perry (1995) defined two distinct types of eddies to describe the energy-containing motion within a turbulent boundary layer. Type-A eddies are considered wall structures and produce finite Reynolds stress at the wall, while Type-B eddies are wake structures and give a zero Reynolds shear stress at the wall. They postulate that these two variations of eddies can account for all possible boundary layer states including both equilibrium and non-equilibrium boundary layers. Ellsberry et al. (2000), noted that boundary layers maintained close to separation over extended distances give rise to nearly linear streamwise growth of integral length scales, and that the boundary layer maintained in a non-equilibrium state required different scales to collapse the velocity and turbulence intensity profiles. Castillo and George (2001) commented further saying that most turbulent boundary layers appear to be equilibrium similarity boundary layers when the pressure gradient parameter Λ = constant, contrary to classical belief that equilibrium flows are difficult to achieve. Further, there are basically three values associated with the pressure gradient parameter defining adverse, favorable, and zero pressure gradient equilibrium conditions. More recently, Schatzman and Thomas (2017) concluded that for turbulent boundary layers exposed to adverse pressure gradients of sufficient magnitude to give rise to an inflectional mean profile, the flow is largely governed by the existence of an outer embedded shear layer. They also stated that separation is not required for the existence of the embedded shear layer, which gives rise to the ability to create a scaling parameter based off of outer flow features.

The primary focus of the present experimental investigations is to characterize the dynamics of the flow naturally approaching separation at the upstream edge of a diffuser duct as well as delayed separation within the duct due to the application of flow control by high-frequency fluidic actuation. The underlying dynamic and structural features of the flow near separation are investigated using conditional averaging, spectral analysis, and proper orthogonal decomposition.

Figure 1. *Flow separation at the entrance to a diffuser duct, illustrated by a contour plot of the measured spanwise vorticity.*

II. Experimental Setup and Methodology

The present experimental investigation is focused on the flow separating in an adverse pressure gradient created at the inlet to a diffuser duct, which is schematically shown in Figure 1. A single field of view measured by particle image velocimetry indicates strong inlet flow separation that constricts the flow passage into the duct. It has been shown (Peterson et al., 2016) that active flow control can be utilized to delay flow separation proportionally with the flow control parameter. Consequently, the fraction of the main flow diverted into the duct, can be tuned by the flow control
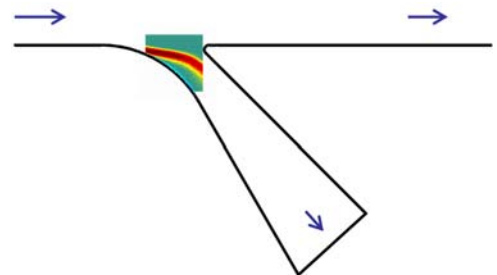
parameter. Nonetheless, the controlled flow still undergoes separation further into the duct, due to the adverse pressure gradient. This work aims at assessing the flow separation under the two most disparate conditions of the prior study (Peterson et al., 2016), namely the base (uncontrolled) flow separation and that of the controlled flow with the longest separation delay at the oncoming $M_o = 0.4$.

All the experiments are performed in a small, open-return, subsonic wind tunnel that is driven by a 75 HP blower, where the temperature of the return air is controlled using a low pressure drop heat exchanger. The tunnel terminates in a nominally free jet discharge station that is coupled to a test geometry. The test geometry (Figure 2) consists of an inlet duct of $W \times H = 2H \times H$ cross-section, where the channel height $H = 76.2$ mm. A diffuser duct branches off from the primary at 45°, while having a lower wall diverging a further 15°, effectively splitting the test section into the primary upper and secondary diffuser duct. The diffuser duct throat is 47.9 mm, while the exit plane is 122.7 mm on the in-plane side shown in Figure 2. The upper surface of the diffuser duct mates to the surface of the primary channel using a 12.7 mm diameter bullnose fit. The flows at the exit planes of both ducts form free jets that are ultimately turned back to the blower's inlet through a settling chamber.

Active flow control utilizes the same flow control components, fluidic oscillating jets, which were applied by Peterson et al. (2016). These jets combine the benefits of unsteady flow control due to their oscillating nature and a net addition of mass and momentum to the flow. Their simplicity of operation and low maintenance requirements make them suitable candidates for airborne applications. These jets are deployed in the current study at a constant streamwise location x, across the span of the lower entrance to the branched duct (Figure 2a), as an array comprised of 23 jets. Their downstream positioning location x is determined by tufts visualization of the flow separation, assisted also by static surface pressure profiles over the smooth base flow control module (not shown). The jets, which orifices measure 0.5×1 mm on the sides are spaced 6.4 mm apart and their nominal issuing direction is tangential to the surface moldline, while they oscillate in the spanwise direction. The jet oscillating frequency is a weak function of the supplied flow rate to the jet and, for typical flow rates utilized in the current test, the frequency is on the order of 10 kHz, as bench-tested by a hotwire anemometer. The actuation strength (or flow control parameter) is characterized using the mass flow rate coefficient C_q, which is the ratio of the total mass flow rate through the jet array and the incoming mass flow rate. The incoming flow at the test section inlet cross section is characterized by the Pitot probe at $x = 0$, and the corresponding Mach numbers define the inlet flow condition M_o, along with the temperature measured by a transducer mounted in the surface of the inlet wall.

Particle image velocimetry (PIV) is the main diagnostic tool used for characterizing the separation dynamics. For that purpose, the PIV laser sheet passes through the optical window,
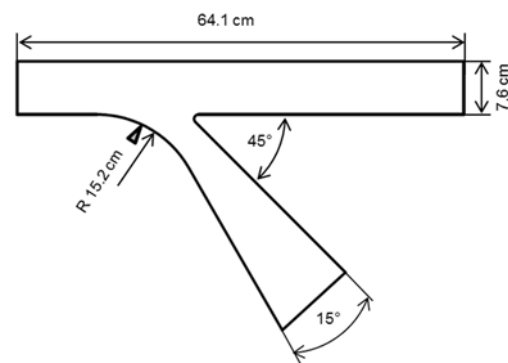

Figure 2. *Flow geometry (duct depth is 15.2 cm). Flow control streamwise position is marked by the triangle.*

4

illuminating the central vertical plane. One side wall of the test section is made of acrylic, and the PIV camera is positioned parallel to that side plane and mounted on a computer controlled x-y traversing mechanism. Three PIV fields of view are utilized in the current investigation. The largest view spanned about 0.95H and is typically used to capture the entire extended flow fields in

Figure 3. *Raster plots of the mean vorticity with overlaid mean velocity profiles for the base (a) and the controlled flow (C_q = 0.8%) (b), for M_o = 0.4. Dashed rectangles represent nominal fields of interest for the local flow separation.*

multiple, partially-overlapping measurements in order to preserve the resolution of the single window measurements over the entire domain. Such PIV data sets are acquired at 500 Hz. While useful in gaining insight into global flow features, such as the mean separation location, resolving the flow about separation required enhanced spatial (and temporal) resolution. Highly-resolved PIV measurements are then taken centered about the local flow separation in the mean sense. As the local flow separation becomes delayed under flow control, the two nominal, higher resolution, PIV windows for the base (uncontrolled) and the flow controlled by C_q = 0.8% are displaced from each other, as illustrated in Figure 3. The size of these nominal measurement domains is only 0.28H. It should also be noted that these two flow domains of interest are under different adverse pressure fields as flow control migrates the separation along the entrance geometry into the diffuser duct, where the controlled flow separates again. Finally, when examining spectral properties of the flow fields about the separation point, only the field of view with highest resolution is utilized, measuring only 0.06H. In addition to the high spatial resolution, these measurements also have high temporal resolution, as the PIV data is recorded at 5 kHz.
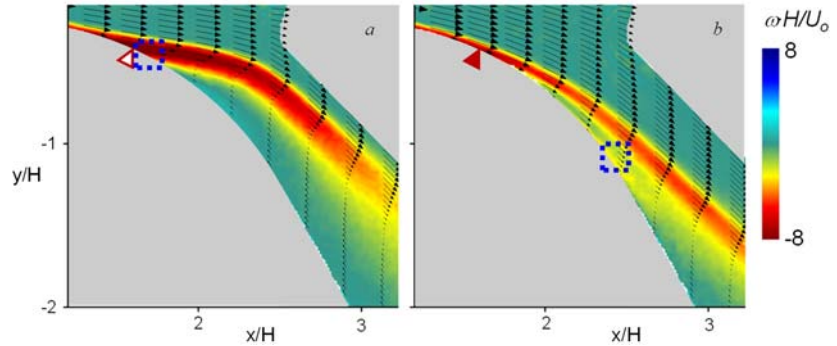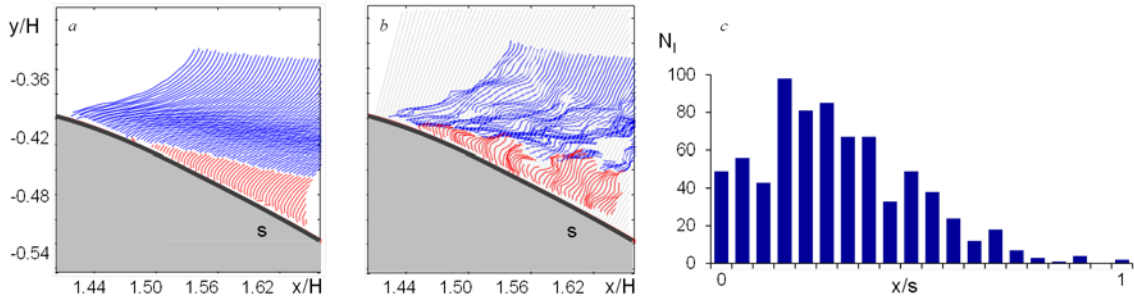

Figure 4. *Ensemble-averaged (a) and instantaneous (b) velocity profiles of the base flow at M_o = 0.4. Reversed portions of the flow are colored in red. Corresponding histogram of the flow separation location along the surface is shown in (c).*

III. The Base Flow

Detailed characterization of the global base flow, and the associated pressure fields, under the varying oncoming Mach numbers were presented by Peterson et al. (2016). Here, the focus is on the flow separation unsteadiness, as measured within the dashed domain shown in Figure 3a, and at M_o = 0.4. First, the mean velocity profiles are shown in Figure 4a, in the local wall-normal coordinates. The mean profiles are colored such that the reverse portion of the flow is shown in red. Note that the base flow separates at about less than one-third of the streamwise distance s

5

captured in this nominal field of view. Each of the mean flow fields is based on 800 instantaneous PIV measurements that indicate significant displacement of the instantaneous separation point. One of such instantaneous flow fields in shown in Figure 4b, in which the separation point moved upstream from its mean location. Each set of the instantaneous velocity flow fields is processed in search for the incipient separation point along the wall, and the separation point distribution is binned along the full streamwise span *s*. The resulting separation histogram for the base flow at $M_o = 0.4$ is shown in Figure 4c. First, it is seen that the natural separation traverses the whole streamwise extent along the wall, although rarely stretching to the farthest downstream location. Second, this distribution clearly indicates a preferential separation location that coincides with the mean location shown in Figure 4a. This separation binning technique is also used for conditional averaging of the flow fields, relative to the flow separation location, for both the base and controlled flows.
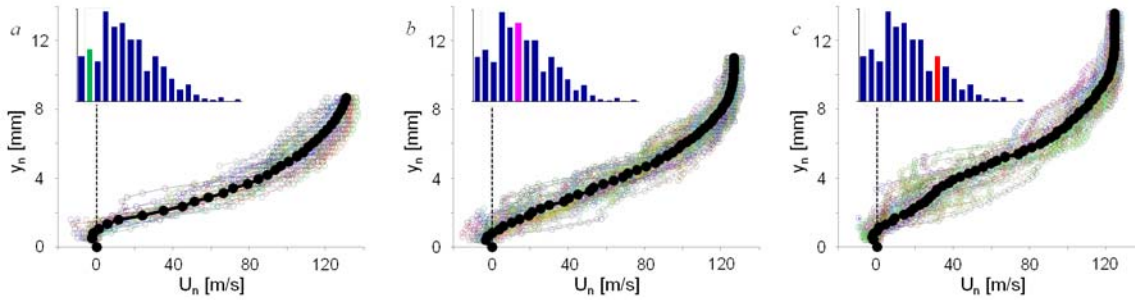

Figure 5. *Binned wall-tangential velocity profiles for the upstream (a), mid (b), and downstream (c) base flow separation, based on the separation location binning of Fig. 4. Bin-averaged profiles are overlaid in solid symbols. Inset plots highlight each bin position.*

The conditional-averaging technique is illustrated in Figure 5 for the base flow examined in Figure 4. Three instances are selected, each representing incipient flow separation, as it moves through the given measurement domain. Figure 5a illustrates conditionally-averaged velocity profiles of the flow separating next to the most upstream position of the field of view, which is marked by the highlighted histogram bin that is utilized for the velocity averaging. All the velocity profiles detected with this bin are plotted in Figure 5a in open symbols, and the corresponding bin-averaged velocity profile is shown in solid symbols. Analogously, the same procedure of the conditional averaging is repeated for the flow separation close to the most probable location (Figure 5b), and for the case when the flow remains attached for over the midpoint of the streamwise span (Figure 5c). It is clear that each of these three instances captures the very moment when the flow close to the surface reverses its direction, i.e., just as the flow becomes separated, despite being at different domains along the surface. Furthermore, the expected 'stretching' of the velocity profile is seen and progresses as the profiles move in the downstream direction. As the flow remains attached farther along the surface it exhibits reduced shear due to diffusion of the embedded shear layer. As a consequence of flow progressing along the surface, the bin-averaged profiles indicate decreasing slope normal to the wall.

IV. The Controlled Flow Separation

Global effectiveness of the flow control approach in diverting the oncoming flow into the diffuser duct is illustrated in Figure 6. Cross sectional views in the *x-y* center plane of the time-averaged diverted flow are shown for $M_o = 0.2, 0.3,$ and 0.4 in terms of the color raster plots of the spanwise vorticity ω_z overlaid with the profiles of mean velocity vectors. Each of these composite flow
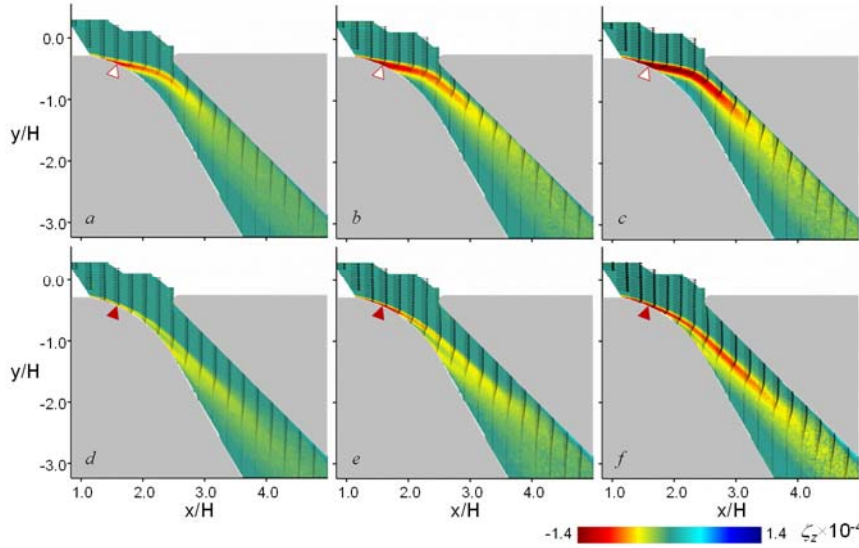
Figure 6. *Contour plots of the mean vorticity with overlaid equidistant mean velocity profiles for the base (a – c) and the flow controlled by Cq = 0.8% (d – f) for M = 0.2 (a, d), 0.3 (b, e), and 0.4 (c, f).*

fields is assembled from ten partially overlapping individual PIV fields of view, such that the composite flow field covers the branched duct from its entrance to close to just upstream of its exit plane (the solid surfaces within the field of view are marked in light gray, and the position of the actuators is marked for reference). The base flow (Figures 6a–c) is marked 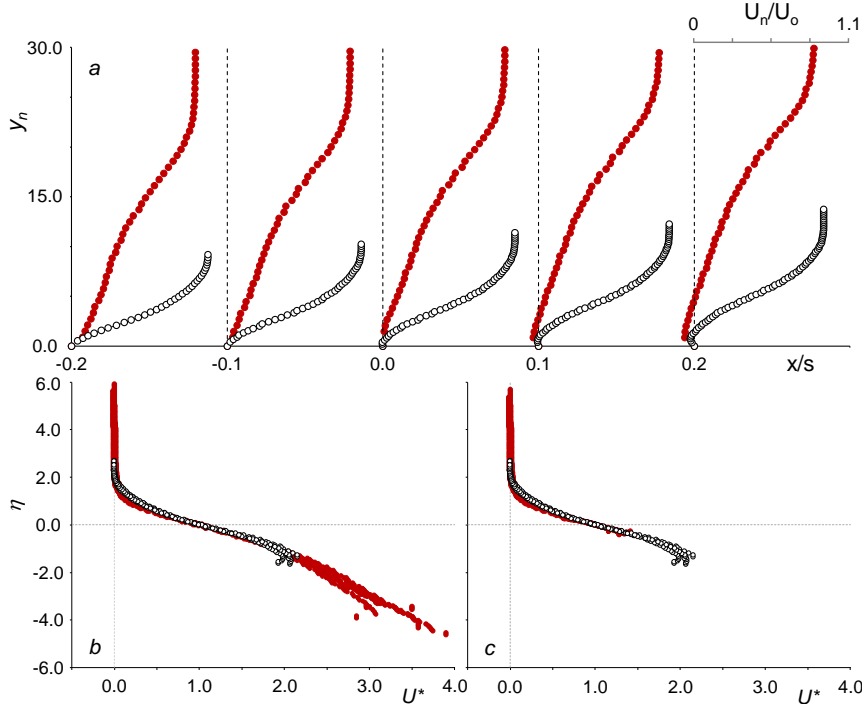by a strong vorticity layer that separates off the convex transition section as a result of the adverse pressure gradient at the inlet to the diffuser duct. The separated shear layer initially follows along the direction of the primary flow and shortly thereafter deflects sharply into the diffuser duct such that the flow is partially constricted by the separated flow domain underneath the shear layer. As the flow that is captured by the diffuser duct is advected downstream, it remains confined by the large separated domain along the lower surface all the way to the exit plane. The effects of fluidic actuation on the global flow field are shown in Figures 6d–f using time-averaged PIV composite velocity and vorticity fields assembled in the same manner as for the base flows. Flow control is adjusted such that the same flow control parameter $C_q = 0.8\%$ is utilized regardless of the oncoming flow Mach number. It is clear that the global features of the controlled flows are similar. The flow remains attached into the duct, however, the extent of the deflection of the separated shear layer towards the bottom surface diminishes somewhat with increasing M_o.

As the main focus of the present work is on the local flow separation, several velocity profiles of the mean flow fields at $M_o = 0.4$ (Figures 6c and f) are extracted about the mean local separation point ($x'/s = 0$), such that two equally-spaced profiles, both upstream and downstream from the central separation profile are shown in Figure 7a, for both the base (Figure 6c) and controlled (Figure 6f) flow. Both velocity profiles indicate a dominant shear-layer-like structure even upstream from separation, which is characteristic of boundary layers in an adverse pressure gradient. The velocity profiles consequently extend farther away from the surface as the controlled flow overcomes the adverse pressure gradient, to the point that they have almost a threefold characteristic scale compared to the base flow. Additionally, the controlled profile develops an additional inflection point closer to the surface, which is referred to as the 'inner', in contrast to the 'outer' inflection point present in both sets of profiles. Characteristic features of the flow approaching separation due to the adverse pressure gradient is that its shear stress at the wall approaches zero, and Elsberry et al. (2000) postulated that this diminishes the importance of the wall region relative to the outer region on the flow approaching separation. Recently, Schatzman and Thomas (2017) proposed a scaling of the adverse pressure gradient flow that, instead of traditional boundary layer wall scaling parameters, utilizes the outer shear layer parameters,

expressed through the shear layer vorticity thickness and velocity defect at the inflection point. They demonstrated excellent scaling of their experimental data and extended it to other available data in the literature. In principle, the proposed scaling was shown to be applicable to different flows undergoing separation due to adverse pressure gradients, with a deviation close to the wall, as can be expected from applying outer scaling parameters.

Figure 7. *Mean velocity profiles (a) of the base (○) and the flow controlled by C_q = 0.8% (●) centered at local separation (x/s = 0), immediately upstream (x/s <0), and downstream (x/s >0) of separation. Scaled mean velocity profiles by the outer shear layer properties (b, after Schatzman and Thomas, 2017) and by dual inner/outer shear layer scaling (c).*

The proposed scaling by Schatzman and Thomas (2017) is applied to the present profiles shown in Figure 7a, where the two

separating flows are markedly different. The controlled flow re-separates under different adverse pressure gradient conditions than the base flow due to the delay of the separation into the diffuser duct. Also, due to significantly delayed separation, the controlled flow velocity profile scale extends much farther away from the surface and develops a secondary inflection point closer to the wall. Nonetheless, when all of the velocity profiles depicted in Figure 7a are scaled by the outer shear layer parameters (after the approach of Schatzman and Thomas, 2017), they still collapse onto a single shear-layer-like profile all the way until the scaling deviates close to the surface, as shown in Figure 7b. It can be noted that the controlled flow scaling begins to deviate off of the scaled profile farther away from the surface than the base flow. This is attributed to the secondary profile inflection, and it is addressed by using a dual inner-outer shear layer scaling of the controlled flow velocity profile. Instead of using the outer shear layer parameters for the full profile, the corresponding inner shear layer parameters are used from the second inflection point located closer to the wall, while the outer scaling is preserved elsewhere. The results of this inner/outer scaling are shown in Figure 7c and appear to reduce deviation of the scaled experimental data towards the surface. Regardless of which scaling is used, it is rather remarkable how robust the shear-layer-based scaling is under the two distinct flows, separating under different adverse pressure gradients.

V. Flow Separation Characteristics

Separation point statistics for the controlled flow separation is extracted from the instantaneous wall-tangential velocity profiles analogous to the base flow separation point characterization (Figure 4). The ensemble-averaged velocity profiles are shown in Figure 8a, having the reversed

American Institute of Aeronautics and Astronautics

flow colored in red. Controlled flow separation is located just below the midspan of the measured flow field in the average. One example of an instantaneous velocity field is shown in Figure 8b, illustrating an instance in time when the flow separation has migrated upstream from its mean position. Instantaneous flow separation points along the surface are extracted for the full set of instantaneous velocity profiles and the resulting histogram showing the separation distribution over the surface is shown in Figure 8c. Similar to the base flow, the flow separation point traverses the whole streamwise extent along the wall. However, contrary to the base flow, no clear preference in the separation location is observed, as the controlled flow histogram appears relatively featureless. This also suggests that the flow separation point oscillations intensify in the controlled flow.
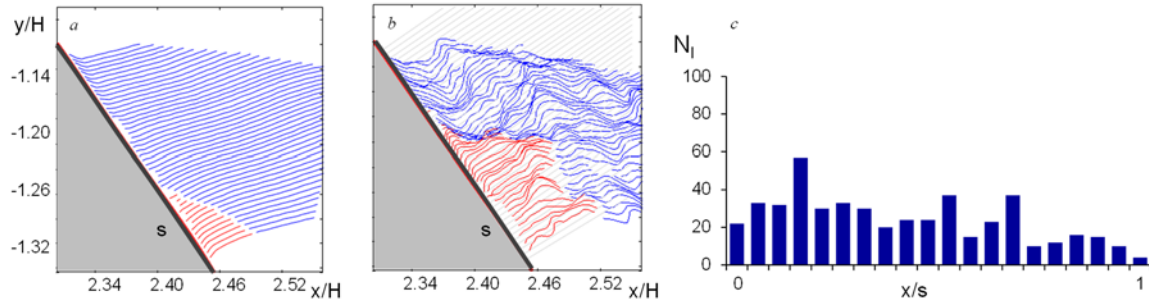

Figure 8. *Ensemble-averaged (a) and instantaneous (b) velocity profiles of the flow controlled by C_q = 0.8%. Reversed portions of the flow are colored in red. The corresponding histogram of the flow separation location along the surface is shown in (c).*

As illustrated in Figure 5 for the base flow, separation histograms for the base or controlled flow can be utilized for conditional flow averaging with respect to the particular bin (streamwise extent) of separation. Such conditional averaging enables examination of the flow evolution through separation for discretized separation locations along the surface. Figure 9 shows three flow evolutions for the base (Figure 9a) and controlled (Figure 9b) flows. Three separation locations are selected for either flow: upstream, downstream, and central, which are color coded in green, red, and blue, respectively. Upon selection of the separation location, four additional, equally spaced, velocity profiles (two upstream and two downstream) are shown. The spacing is determined from the central location in the base flow, and as such, not all velocity profiles under equidistant spacing are contained in the field of view and are omitted. . These conditional velocity profiles capture the progression of separation as the flow passes from immediately upstream to past the separation point. The cross stream extent of the base flow profiles is fully captured within the field of view, and shows an expected growth of the velocity profile as the separation point moves from the most upstream to the most downstream
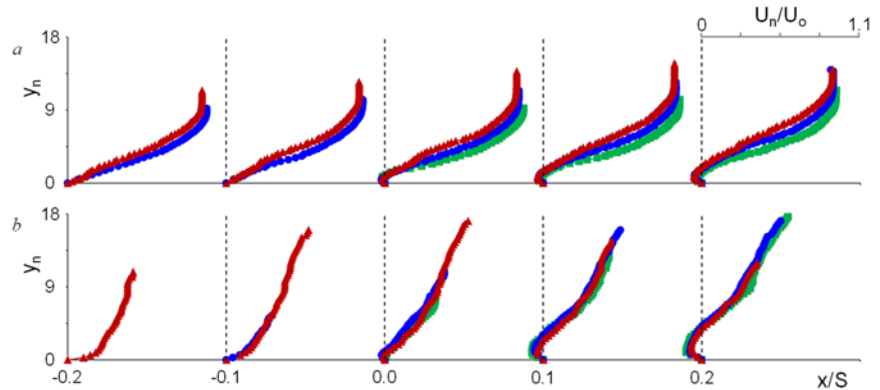

Figure 9. *Conditionally-averaged velocity profiles U_n of the base (a) and the flow controlled by C_q = 0.8% (b) at local separation (x/s = 0), immediately upstream (x/s <0), and downstream (x/s >0) of separation, for the onset of separation progressing from the most upstream (—) to the most downstream (—) location along the surface.*

9

location. Although not done, it is clear that the same outer shear layer scaling applied to the mean velocity profiles (Figure 7b) would collapse these conditionally-averaged velocity profiles as well. Similar to the base flow, the progression of the flow through separation for the controlled flow is shown in Figure 9b. First, as the controlled flow velocity profile cross stream scale extends multifold over the base flow, highly resolved measurements do not capture the full velocity profile in any of the controlled cases. As the flow approaches separation ($x/s < 0$), the controlled profiles indicate increased wall shear compared to the base flow. However, the shear is higher in the base flow elsewhere, outward from the wall.

Conditionally averaged flow fields based on the separation histograms discussed earlier are shown in Figure 10. First, the global measured flow fields are shown in Figures 10a and e for the base and controlled flow, respectively. Contour plots of wall-tangential velocity component U' clearly indicate the separation point in the average sense. To examine the localized dynamics near separation, much smaller fields of view are centered about the mean separation point in either case, marked by a white rectangle (Figure 10 a and e), and highly-spatially resolved PIV measurements are taken in each of the zoomed-in domains that span about 0.28H. The resulting mean flow fields are shown in Figures 10b and f, also in terms of the contour plots of the wall-tangential velocity. Each of these time-resolved measurements is processed in the same manner as already discussed in relation to Figures 4b and 8b, resulting in histograms of the flow separation location along the streamwise span s, as shown in Figures 10c and g. These histograms are utilized to uncover the flow features relative to the separation point, as the separation point moves along the surface, by conditionally-averaging all the flow realizations within a particular bin (i.e., the streamwise position and extent of separation). As an illustration, two instances are selected such that the instantaneous separation remains in the vicinity of the averaged separation are shown in Figures 10d and h, where each selected separation bin is colored red in the corresponding histograms.

The conditionally averaged fields can be used to extract further flow dynamics and parameters. Analysis of the corresponding spatial distributions of turbulent kinetic energy (TKE) is shown in Figure 11. Two contour plots for the larger global views for the base and controlled flows are shown in Figures 11a and d, respectively. Although the flow separates (in the mean sense) within the field of view, a continuous band of vorticity is measured across the whole field of view, which intensifies beyond the separation point, as already shown in Figure 3. A notable vorticity layer,
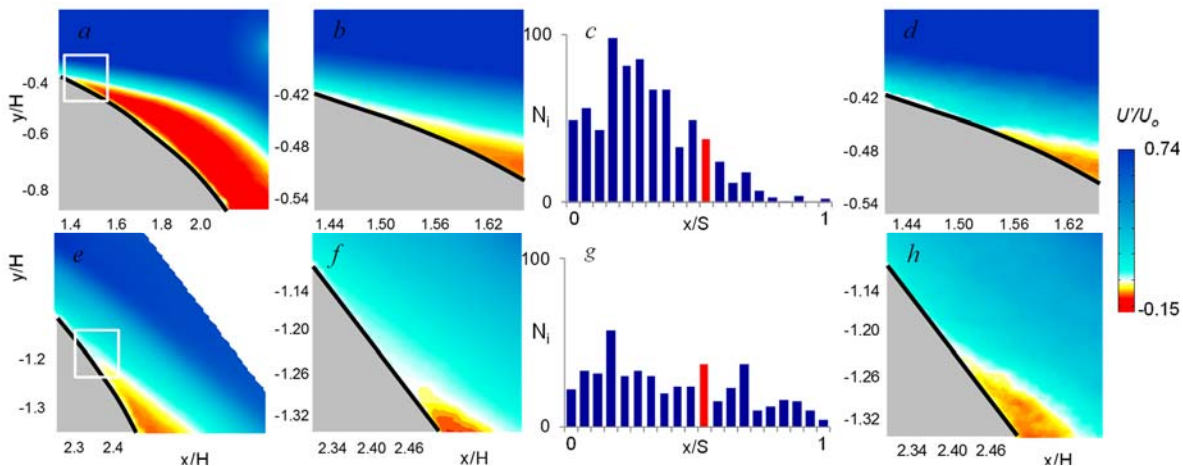

Figure 10. Contour plots of the averaged wall-tangential velocity U' for the global (a, e) and local (b, f) fields of view. Conditionally-averaged U' is shown in (d, h) for the median bin of the separation location histogram (c, g). Base (a–d) and the flow controlled by $C_q = 0.8\%$ (e–h) are characterized at $M_o = 0.4$.

10

displaced from the surface, is induced by the bound shear which is discussed in Figure 7. The global flow views in Figures 11a and d indicate that distributions of TKE are closely aligned with vorticity distributions shown in Figure 3. Once the flow separates and the shear layer forms, enhanced flow entrainment and mixing increases the level of turbulent kinetic energy. When the kinetic energy distributions are extracted from the high-resolution PIV measurements within the domains marked by white rectangles in Figures 10a and e, more details about the local turbulent kinetic energy distribution between the base and controlled separation, are seen in Figures 11b and e. In each of these two views, the flow separation is located close to midway of the streamwise span, in the average sense (cf. Figures 10b and f). Regardless, the base flow is marked by an uninterrupted TKE layer above the surface, which only begins to intensify as the free shear layer forms past the flow separation. Similar TKE evolution is seen past separation in the controlled flow (Figure 11e), although the cross stream expanse of the TKE is much larger corresponding to the increase in cross stream stretching and extended shear of the velocity profiles in the controlled flow. Additionally, it can be noted that the absolute TKE levels about separation are increased in the controlled case, relative to the base flow. Finally, if TKE is conditionally averaged relative to the separation point, for the same highlighted bins as shown in Figures 10c and g, pseudo-instantaneous features of TKE distributions, relative to the separation location, are brought into the forefront (Figures 11c and f). The signature of the enhanced TKE in the separating shear layer becomes more isolated from the bound vorticity of the attached upstream flow in the conditional averages. Conditional averages still indicate that the TKE levels at the separation point (and immediately downstream from it) are higher for the controlled (Figure 11f) than for the base (Figure 11c) flow.

Further statistics of the flow separation are based on examining wall-tangential velocity distributions along the surface, as both sign and magnitude of the velocity point to instantaneous flow separation, in reference to the given point in the flow. The methodology of this statistical approach is outlined in Figure 12. First, to gain more insight into statistical nature of the flow separation, spatial histograms of the reversed flow coefficient γ are shown in Figures 12a and e, for the base and controlled flow, respectively. For each of the measured wall-tangential velocity components, γ is a fraction of instances when that velocity was aligned with the reversed flow; $\gamma = 1$ meaning that the flow is separated for all instances. There are several differences that can be pointed out when comparing the base and controlled flow histograms. In the base flow, the flow reversal is confined within a closer proximity of the surface, and the flow remains separated most of the time in the downstream part of the reversed flow. This also agrees with the earlier analysis in Figure 4c,
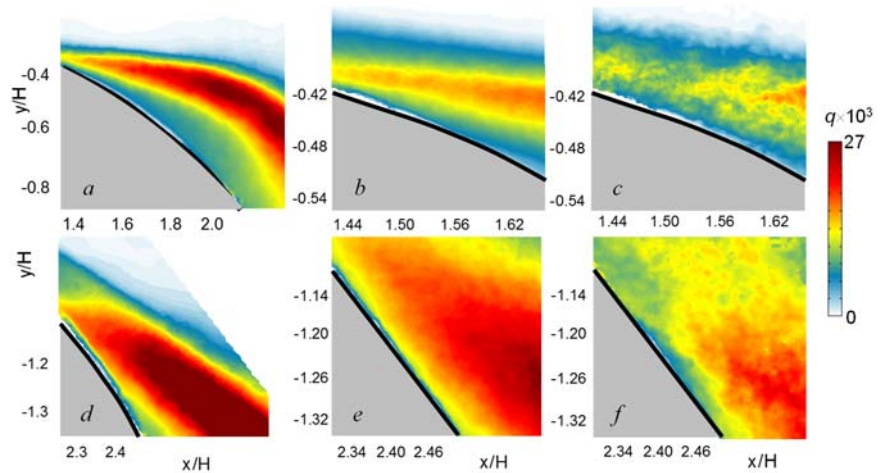

Figure 11. *Contour plots of the turbulent kinetic energy q for the global (a, d) and local (b, e) fields of view. Conditionally-averaged q is shown in (c, f) for the median bin of the separation location histograms (Fig. 10c, g). Base (a–c) and the flow controlled by $C_q = 0.8\%$ (d–f) are characterized at $M_o = 0.4$.*

11

highlighting that the separation location along the surface has a clear peak, although it spread throughout the domain. In contrary, controlled flow reversal appears to spread outward almost to the full extent of the field of view, and not even the far downstream domain is separated at all the instances. This indicates a need for a more globalized measure of the flow separation, rather than the surface location discussed in Figure 8c. The increased spatial extent of reversed flow suggests more complex dynamics of the flow separation in the controlled flow. The first step in the analysis of the flow reversal pertained to filtering of the small-scale motions that could trigger erroneous detection of the flow separation. Therefore, the flow fields are first low-pass filtered using the POD reconstruction, where only the first three dominant modes are retained. The POD-reconstructed flow fields are processed at the reference point in each of the flow fields, marked in Figures 12b and f by a plus sign, yielding histograms of the wall-tangential velocity component. The resulting histograms for the base and controlled flows are shown in Figures 12c and g, respectively. As the base flow has a smaller extent of the separation point displacement, the developed histogram has a correspondingly narrow velocity distribution. The most probable velocity appears to be nearly zero, as the selected point is right about the separation point (Figure 12b). A broader range of the realized wall-tangential velocities for the controlled flow histogram (Figure 12g) points to increased displacement of the separation point. The most probable realization has a small positive velocity, indicating that the selected point is just upstream from separation on the average sense (as also seen in Figure 12f). Just as in the case of the histograms of the surface separation point distribution, the present histograms are utilized for conditional averaging of the flow fields based directly on the binned wall-tangential velocity range. Indirectly, this binning relates to the flow separation, and the POD-reconstructed field exhibits a continuous relationship between the flow separation location and the velocity field, void of small-scale disruptions. To demonstrate the application of the velocity histograms to conditional averaging, two different regions of the histograms are selected for the base and controlled flows, each of them highlighted in Figures 12 c and g. The velocity span for the base flow is selected to be within the positive range, implying flow attachment beyond the reference point. This further suggests that
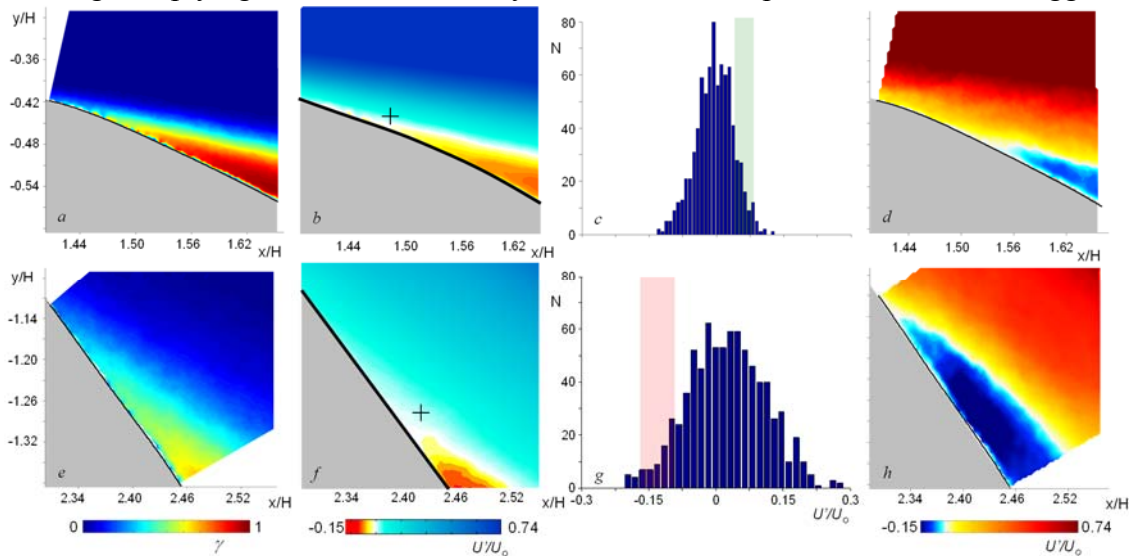

Figure 12. *Spatial histograms of flow reversal for the base (a) and controlled flow (e). Contour plots of the averaged wall-tangential velocity U' for the local (b, f) fields of view for the base (b) and actuated flow (f). Histograms of the wall-tangential velocity near separation based on 3 mode POD reconstruction for the base flow (c) and actuated flow (g). Conditionally averaged wall-tangential velocity contour plots selected based off of the histogram criteria showing ability to locate separation along the surface for base (d) and controlled flow (h).*

12

the flow conditionally averaged over this extent would separate only towards the downstream end of the measured domain. Indeed, once the averaging is done, and the corresponding contour plot of the wall-tangential velocity is shown in Figure 12d. It is clear that the flow stays attached past the mean flow separation. In the case of the controlled flow, a region of interest is selected such that the velocity sign is not only negative, but also closer to the tail end of the distribution (Figure 12g). This indicates that predominantly strong reversed flow is measured at the point, which in turn suggests that the flow separation commences far upstream from the considered reference point near the mean separation. After the flow fields are conditionally averaged, the corresponding contour plot of the wall-tangential velocity clearly indicates that the flow separation begins close to the most upstream location of the field of view. Therefore, the histograms of the POD-reconstructed velocity are to be considered as a further global measure of the separation location to extract relevant flow features.

Three conditionally-averaged flow fields are created for both the base and controlled flow, as the averaging bin is shifted from the negative to positive range of the U' histograms in Figures 12d and h. The resulting contour plots for U' and V' velocity components for the base flow are shown in Figures 13a,e,i and 13b,f,j, respectively. These conditional averages show an upstream to downstream progression of separation in the base flow and serve as anchoring points for further analysis of other flow parameters as separation migrates in the field of view. Conditionally-averaged vorticity fields are shown in Figures 13c,g,k, following the downstream progression of separation. The vorticity levels decrease as separation shifts, which is attributed to the extending velocity profiles in the downstream direction, which reduce shear and hence result in lower
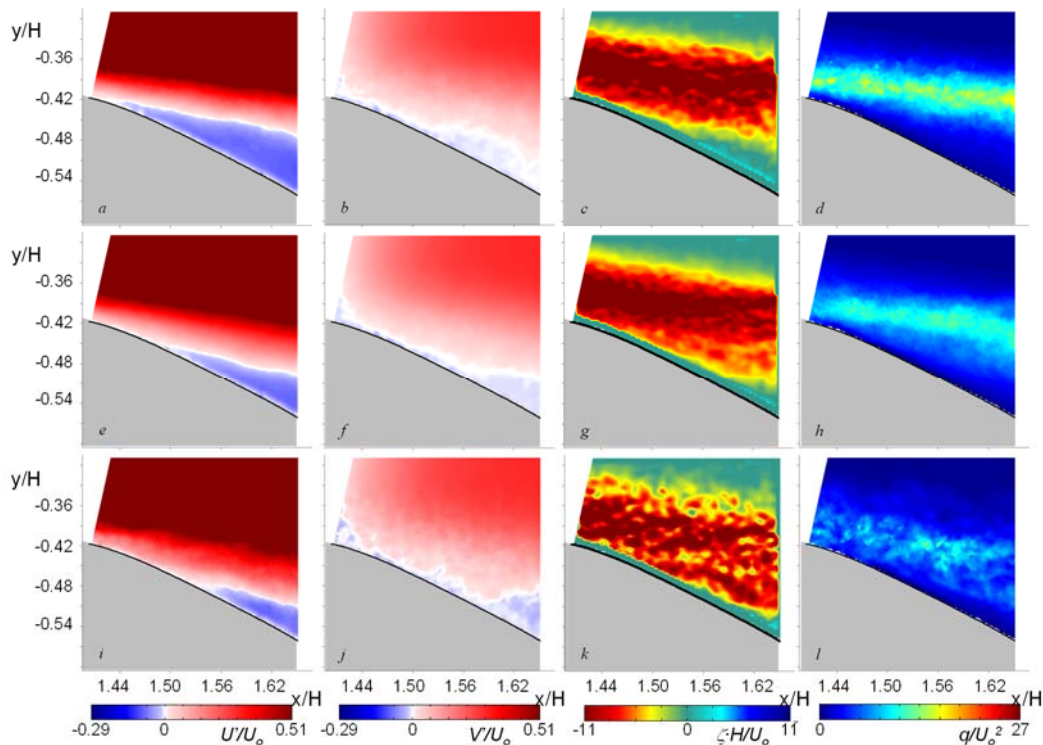

Figure 13. *Conditionally averaged flow field quantities for varying separation location of the natural separation determined from the global criteria developed using POD reconstruction. Separation moves downstream from top to bottom row. Contours of wall-tangential velocity U' are shown as separation moves downstream (a,e,i). Other quantities shown are wall-normal velocity V' (b,f,j), vorticity (c,g,k), and turbulent kinetic energy (d,h,l).*

13

vorticity magnitudes. Corresponding features of the turbulent kinetic energy evolution are shown in Figures 13d,h,l and are in line with vorticity observations. As the flow separates at the most upstream location (Figure 13d), larger shear increases production on TKE, which is sufficiently away from the viscous wall layer and cannot be balanced by dissipation. This excess TKE is therefore convected (among other transport mechanisms) and manifests itself in increased TKE levels in the forming stages of the shear layer. As the separation moves in the downstream direction, TKE levels become more of a signature of the convected TKE from the upstream embedded shear layer, and signature peaks of the separating shear layer become displaced outside of the field of view. This is particularly visible for the farthest-separating case (Figure 13l).

Analogous to the base flow analysis in Figure 13, three conditionally-averaged cases are considered for the controlled flow as flow separation shifts downstream, which is seen in the U' and V' contour plots in Figures 14a,e,i and 14b,f,j, respectively. Although the corresponding vorticity concentrations (Figures 14c,g,k) become much more diffused in the controlled flow, they still follow the same trend seen in the base flow analysis: as the flow separation shifts downstream, vorticity concentrations diminish, as the extended velocity profiles upstream from separation approach near-zero shear considerable distances away from the wall (see Figure 7a). Contrary to the base flow evolution, turbulent kinetic energy of the controlled flow appears to increase with the downstream shift in the flow separation, as seen in Figures 14d,h,l.

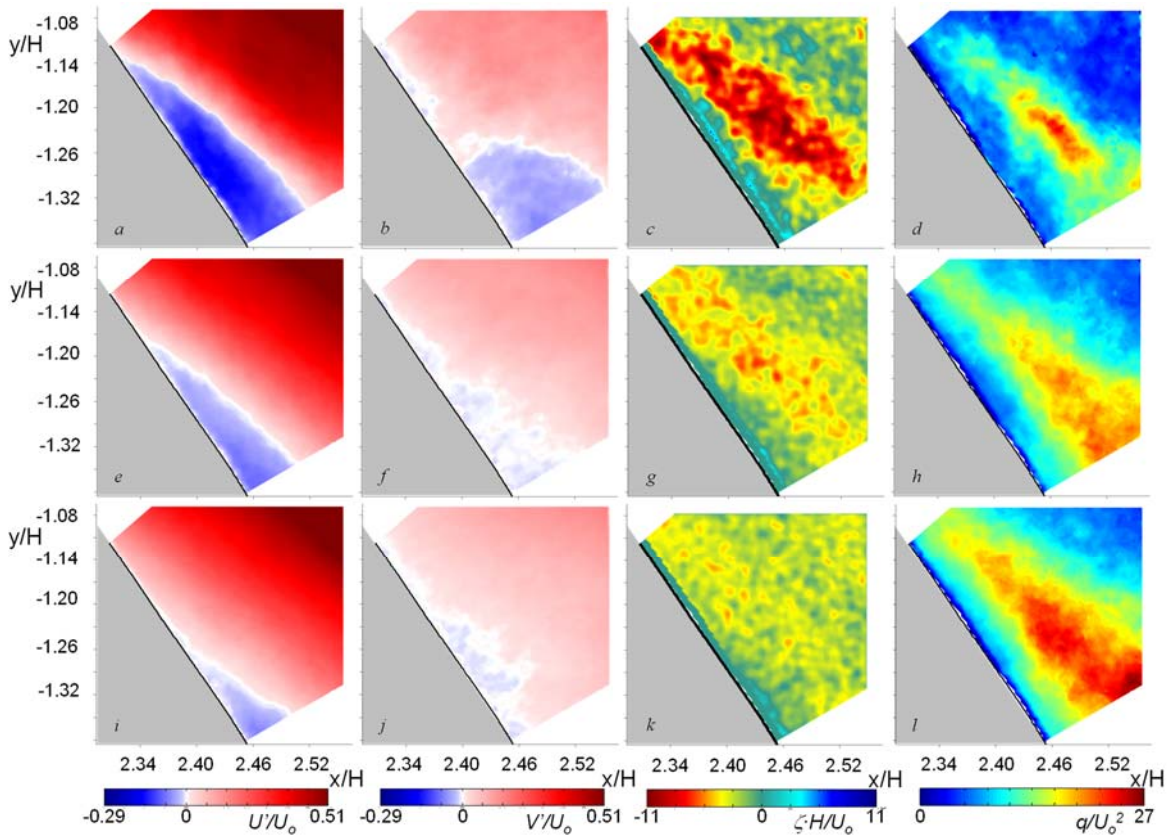## VI. Flow Structure at Separation

Figure 14. *Conditionally averaged flow field quantities for varying delayed separation location of the actuated flow determined from the global criteria developed using POD reconstruction. Separation moves downstream from top to bottom row. Contours of wall-tangential velocity U' are shown as separation moves downstream (a,e,i). Other quantities shown are wall-normal velocity V' (b,f,j), vorticity (c,g,k), and turbulent kinetic energy (d,h,l).*

Previous measurements pointed to an increase in turbulent kinetic energy about separation in the controlled flow, despite successful scaling of the mean velocity profiles through the flow separation for both flow conditions, as shown in Figure 7. This section further examines the similarities and differences in the flow dynamics about the local separation point in the absence and presence of actuation. For further examination, the PIV field of view is set to only about 5 mm × 5 mm about the local separation point and sampled at 5 kHz. For reference, this highly-resolved measurement yields about five equally-spaced velocity time traces over the same span a typical miniature hot-wire sensor that is 1.25 mm long (and 5μm in dia.) would resolve. To further illustrate the size and location of these miniature PIV measurement domains, their bounds are marked by dashed rectangles in the nominal $0.28H$ measurement domains that were utilized in prior analysis. They are overlaid on contour plots of the turbulent kinetic energy for the base (Figure 15a) and controlled flow (Figure 15b). Ten PIV measurements are conducted over one second intervals, and the individual velocity fluctuation spectra at each measurement point are averaged over these realizations for suppression of random noise levels. Upon examination, the spectral content of the velocity fluctuations appeared similar throughout each interrogation domain, presumably due to the small overall measurement domain. Therefore, only a single characteristic spectrum is shown in Figure 15c for the base and controlled flow interrogation domains. Although the frequency bandwidth up to 2.5 kHz is not sufficient to capture all relevant scales of the velocity fluctuations, it is sufficient to capture a full range of energy-bearing motions.

The energy-bearing scales of the base flow stretch over the entirety of the resolved range of scales, while in the controlled flow, part of the inertial range (close to -5/3 slope) is contained within the resolved frequencies. Two main differences are pronounced when comparing the two spectra. First, a significant increase in large-scale motions is evident in the controlled flow, relative to the base flow, as the power contained in the lower frequencies is higher. Secondly, the controlled flow also begins to transfer energy to the smaller scales at lower frequencies, which leads to a dropoff in energy content over its inertial range. Although the presently resolved scales indicate about the same energy levels at the highest resolved frequencies, it is not difficult to infer that there is a crossover at
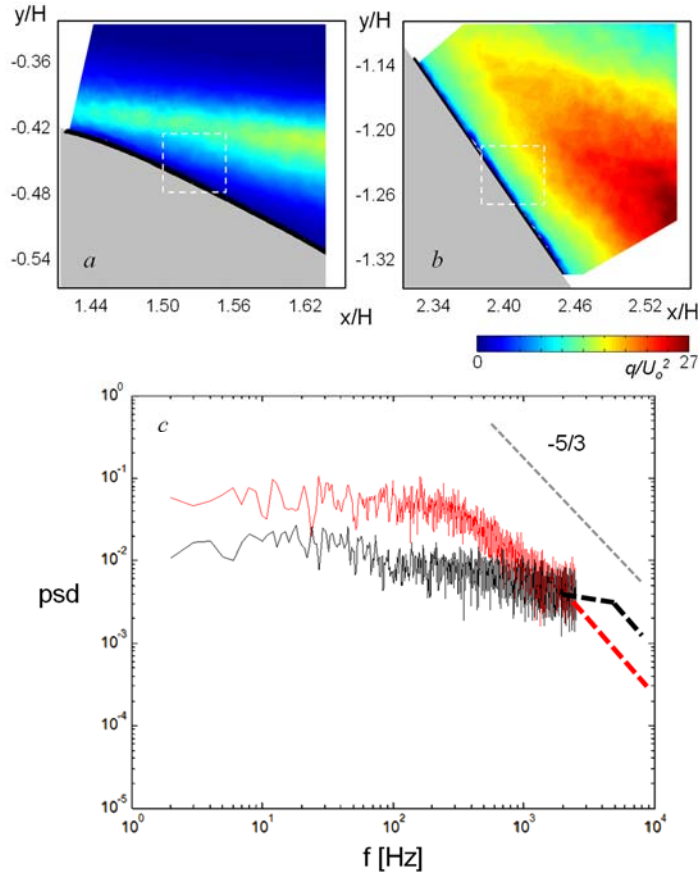

Figure 15. *Contour plots of the turbulent kinetic energy q for the base (a) and the flow controlled by C_q = 0.8% (b) at M_o = 0.4. Power spectra of velocity fluctuations (c) measured within dashed windows in (a,−) and (b,−).*

15

a higher frequency range than contained in these measurements, beyond which, the energy content of the small scales in the base flow would be higher than that of the controlled flow. This point is emphasized by the dashed extensions of the measured power spectra.

Further insight into the flow dynamics in the absence and presence of actuation is investigated using proper orthogonal decomposition (POD, Sirovich, 1987, Berkooz et al., 1993) of the instantaneous vorticity fields to extract modes of the flow, such that

$$\vec{\omega}(t) = <\vec{\omega}> + \sum_{m=1}^{N} a_m(t) \cdot \vec{\varphi}_m \qquad (1)$$

where $\vec{\omega}(t)$ is the instantaneous vorticity vector, $<\vec{\omega}>$ is the mean velocity field, and $\vec{\varphi}_m$ and $a_m(t)$ are the mth POD mode and its time coefficient, respectively. In the present investigation, only the spanwise vorticity component ω_z is used. The POD modes are ordered by corresponding modal energy contributions (when the flow is dominated by organized, large-scale vortical structures, a few modes are typically sufficient to capture the dominant time-dependent dynamics). The energy contribution of each mode $\vec{\varphi}_m$ is quantified in terms of its eigenvalue λ_m

$$E_m = |\lambda_m|^2 / \sum_{i=1}^{N} |\lambda_i|^2 \qquad (2)$$

Comparison between the modal structures of the two flows about separation is shown in Figure 16. For that purpose, the structure of the first six vorticity modes is shown for the smallest measurement domains (see Figures 15a and b) of the base (Figures 16a–f) and controlled (Figures 16g–l) flows. A striking feature of these two sets of higher order modes is that there are no distinct differences among the two flows. All of the controlled flow modes predominantly appear as tilted and stretched counterparts of the base flow modes, indicating essentially the same dominant structure of the mean flow perturbations near separation in either flow. Switching between the fourth and fifth modes between the two flows is also of lesser importance to the underlying structure. It should be noted that some of the dominant modes resemble organized vortical motions, while the others presumably represent only vorticity layers that do not necessarily correspond to an organized vortical motion. To fully capture the vortical structure an enlarged field of view might be necessary, as the largest relevant modes extend past the boundaries of the current view. Nonetheless, the significance of the modal similarity is twofold: first, it supports the findings about the scaling of the mean velocity profiles between the two flows at separation (Figure 7) and second, it connects the implied similarity of the inviscid instability of the embedded shear layer to the similarity of the organized structures in the flow going through separation.
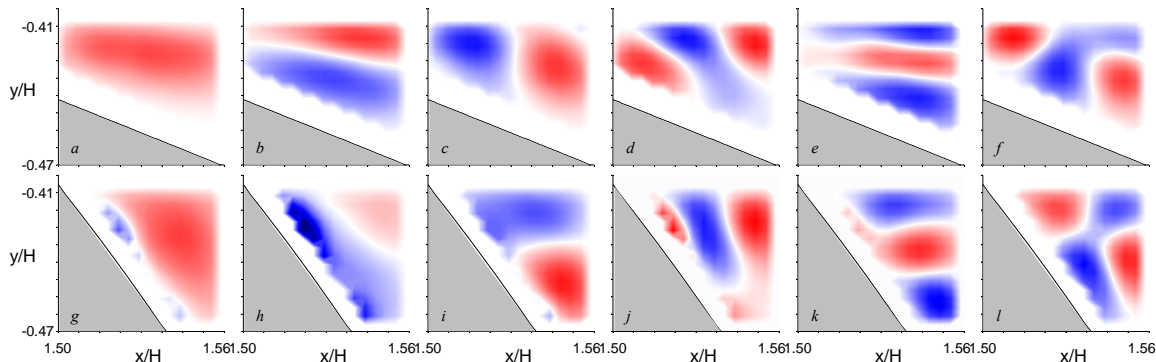

Figure 16. *First six vorticity POD modes for the base (a–f) and the controlled flow (C$_q$ = 0.8%) (g–l) at M$_o$ = 0.4.*

As already suggested by the differences observed in the turbulent kinetic energy (Figure 11) and spectral energy distribution (Figure 15c), it can be expected that the energy composition of the dominant vorticity modes for the two flows would differ, in spite of their structural similarity. Energy fractions of the first twenty POD
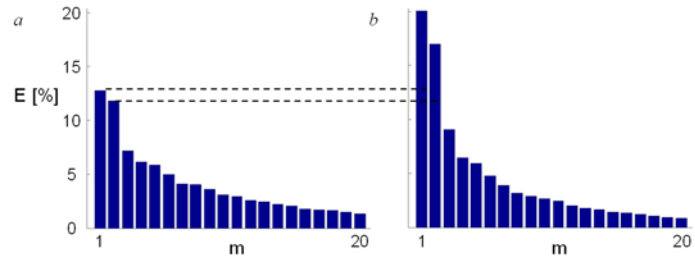

Figure 17. Energy fractions of the first twenty vorticity POD modes for the base (a) and the flow controlled by $C_q = 0.8\%$ (b) at $M_o = 0.4$.

pods are shown in Figure 17 for both flows. Although both of these distributions indicate that the first two modes (Figure 16) carry the most significance with respect to their overall energy fractions, they gain notably more prominence in the controlled flow (Figure 17b). The energy fractions of the modes do not carry information about the absolute difference in energies between the two flows. It can be argued, however, that based on the increased TKE distributions and power spectra, that the overall energy captured in the controlled flow would be higher than that of the base flow. This increase in overall energy would be expected to manifest itself in a large differentiation between the flow fields, although it seems, upon decomposition of the flows, to only increase the prominence of the low order modes, further indicating the lower order modes are tied with the larger scale motions containing more energy in the spectral analysis of the velocity fluctuations about separation.

VII. Conclusions

The dynamics and characteristic structure of natural and deliberately-delayed, migrated separating flow within an adverse pressure gradient imposed by an aggressive diffuser duct are investigated experimentally. The streamwise position of separation is regulated by fluidic actuation of controllable momentum that is applied at the flow boundary ($M_o = 0.4$) using a spanwise array of fluidically-oscillating jets (Peterson et al., 2016). The evolution of separation in the absence and presence of actuation is characterized using planar high-speed PIV (up to 5,000 fps) at several levels of spatial resolution. The global flow field is mapped using composites of individual views that yield the time-averaged domain of separation at it migrates in the streamwise direction when the actuation level is increased. High-magnification views (down to 0.06H) centered about the location of the time-averaged separation are used to assess its spatial and temporal dynamic characteristics. Details of the instantaneous incipient dynamics of the velocity and vorticity fields are examined using conditional averaging, spectral analysis, and proper orthogonal decomposition.

In the presence of actuation, the flow attachment within the diffuser is extended and, consequently, the characteristic cross stream scale of the separating velocity distribution increases significantly as the separation migrates downstream. The cross-stream distributions of the time-averaged streamwise velocity (in the wall-normal coordinates) in the base and controlled flows are dominated by a shear layer between the external core flow and the inner flow near the surface that is characterized by a local inflection point, while the inner flow near the migrated separation develops an additional inflection point close to the surface. The vanishing (time-averaged) shear stress at the surface prompted Elsberry et al. (2000) to postulate that the importance of the wall region relative to the flow dynamics at separation diminishes in comparison to the effects of the outer shear layer flow. The significance of the outer 'embedded' shear layer was formulated by the velocity profile scaling proposed by Schatzman and Thomas (2017). The present

investigations demonstrate that this scaling applies to the cross-steam distributions of the streamwise velocity in spite of the significant disparities in the local cross stream scales, curvature of the surface and the varying adverse pressure gradient. In addition, the present investigations also show that a dual, inner/outer shear layer scaling can further improve the collapse of the velocity distributions even when the flow develops the secondary, inner, inflection point near the surface. Regardless of whether an 'outer' or 'inner/outer' scaling is used, it is remarkable that the separation under different conditions can be scaled by the local vorticity and velocity thickness relative to the inflection point(s).

The similarity of the mean shear velocity profiles implies similar underlying instabilities and ensuing flow structures. The spectral analysis of velocity fluctuations about the local separation domain indicates that as the separation is migrated downstream and its characteristic cross stream scale increases, the energy of the large-scale motions increases and the cascade to small-scale (dissipative) motions occurs at spectral components having lower frequencies (or larger scales). However, proper orthogonal decomposition (POD) analysis of the highly spatially and temporally resolved vorticity field about the local separation of the base and controlled flows shows that the structure of the underlying small-scale flow motions through separation is nearly unchanged as the separation is migrated downstream. In accord with the similarity of the mean velocity distributions the most dominant vorticity modes in the separating flow front appear to simply tilt and stretch relative to the modes of the base flow in the absence of actuation.

References

Amitay, M, Pitt, D., and Glezer, A., "Separation control in duct flows," *J. Aircraft*, **39**, 616-620, 2002.

Banaszuk, A., Narayanan, S. and Zhang, Y., "Adaptive control of flow separation in a planar diffuser," *AIAA Paper* 2003-617, 2003.

Berkooz, G., Holmes, P., and Lumley, J.L., "The proper orthogonal decomposition in the analysis of turbulent flows," *Annu. Rev. Fluid Mech.*, **25**, pp. 539-575, 1993.

Blanckaert, K., "Flow separation at convex banks in open channels," *J. Fluid Mechanics*, **778**, pp. 432-467, 2015.

Burrows, T. J., Gong, Z., Vukasinovic, B., and Glezer, A., "Investigation of Trapped Vorticity Concentrations Effected by Hybrid Actuation in an Offset Diffuser," AIAA Paper 2016-0055, 2016.

Castillo, L. and George, W.K., "Similarity analysis for turbulent boundary layer with pressure gradient: outer flow," *AIAA Journal*. **39(1)**, pp 41-47, 2001.

Chun, Kyung-Bin, and Sung, H. J., "Control of turbulent separated flow over a backward-facing step by local forcing," *Exp. Fluids*, **21**, pp. 417-426, 1996.

Elsberry, K., Loeffler, J., Zhou, M.D., and Wygnanski, I., "An experimental study of a boundary layer that is maintained on the verge of separation," *J. Fluid Mechanics*. **423**, pp 227-261, 2000.

Ethier, C. R., Prakash, S, Steinman, D.A., Leask, R.L., Couch, G.G. and Ojha, M., "Steady flow separation patterns in a 45 degree junction," *J. Fluid Mechanics*, **411**, pp. 1-38, 2000.

Gartner, J., and Amitay, M., "Flow Control in a Diffuser at Transonic Conditions," *AIAA Paper* 2015-2484, 2015.

Gissen, A. N., Vukasinovic, B., Glezer, A., and Gogineni, S., "Active Shock Control in a Transonic Flow," *AIAA Paper* 2013-3116, 2013.

Ho, C.M. and Huerre, P., "Perturbed free shear layers," *Annu. Rev. Fluid Mech.*, **16**, pp. 365-422, 1984.

Kumar,V., and Alvi, F.S., "Use of high-speed microjets for active separation control in diffusers," *AIAA J.*, **44**, pp. 273-281, 2006.

Marusic, I. and Perry, A.E., "A wake model for the turbulent structure of boundary layers. Part 2. Further experimental support," *J. Fluid Mechanics*. **298**, pp. 389 – 407, 1995.

Nishi, M., Yoshida, K. and Morimitsu, K., "Control of Separation in a Conical Diffuser by Vortex Generator Jets," *JSME Int. J B-Fluid T*, **41**, pp. 233-238, 1998.

Papadopoulos, G., and. Otugen, M. V., "Separating and reattaching flow structure in a suddenly expanding rectangular duct," *J. Fluids Eng.*, **117**, pp. 17-23,1995.

Peterson, C.J., Vukasinovic, B., Glezer, A., Saripalli, K.R., and Packard, N.O., "Active Flow Control of Separation in a Branched Duct," *AIAA Paper* 2016-3771, 2016.

Schatzman, D.M., and Thomas, F.O., "An experimental investigation of an unsteady adverse pressure gradient turbulent boundary layer: embedded shear layer scaling," *J. Fluids Mechanics*, **815**, pp. 592-642, 2017.

Simpson, R.L., "Turbulent boundary-layer separation," *Annu. Rev. Fluid Mech.*, **21**, pp. 205-231, 1989.

Sirovich, L., "Turbulence and the dynamics of coherent structures. Part I: Coherent structures," *Q. Appl. Math.*, **45**, pp. 561-571, 1987.

Suzuki, T., Colonius, T. and Pirozzoli, S., "Vortex shedding in a two-dimensional diffuser: theory and simulation of separation control by periodic mass injection," *J. Fluid Mechanics*, **520**, pp. 187-213, 2004.

Vaccaro, J.C., Elimelech, Y., Chen, Y., Sahni, O., Jansen, K.E. and Amitay, M., "Experimental and numerical investigation on steady blowing flow control within a compact inlet duct," *Intl J. Heat Fluid Fl.*, **54**, pp. 143-152, 2015.

Vukasinovic, B., Rusak, Z., and Glezer, A., "Dissipative Small-scale Actuation of a Turbulent Shear Layer," *J. Fluid Mechanics*, **656**, pp. 51-81, 2010.

Yang, W., and Kuan, B., "Experimental investigation of dilute turbulent particulate flow inside a curved 90° bend," *Chem. Eng. Sci.*, **11**, pp. 3593-3601, 2006.

Yoshioka, S., Obi, S., and Masuda, S., "Organized vortex motion in periodically perturbed turbulent separated flow over a backward-facing step," *Intl J. Heat Fluid Fl.*, **22**, pp. 301-307, 2001.

Zaragola, M.V. and Smits, A. J., "Mean-flow scaling of turbulent pipe flow," *J. Fluid Mechanics*. **373**, pp. 33-79, 1998.

American Institute of Aeronautics and Astronautics